



## Tension and fatigue behavior of silver-cored composite multi-strand cables used as implantable cables and electrodes

John J. Lewandowski<sup>a,\*</sup>, Ravikumar Varadarajan<sup>a</sup>, Brian Smith<sup>b</sup>

<sup>a</sup> Department of Materials Science and Engineering, Case Western Reserve University, Cleveland, OH 44106, USA

<sup>b</sup> Department of Biomedical Engineering, Case Western Reserve University, Cleveland, OH 44106, USA

### ARTICLE INFO

#### Article history:

Received 22 January 2008

Received in revised form 7 March 2008

Accepted 12 March 2008

#### Keywords:

Composite DFT<sup>®</sup> cables

Fatigue-life

Coffin–Manson–Basquin

Implantable cables

Functional electrical stimulation (FES)

### ABSTRACT

The mechanical behavior of a variety of cable architectures comprised of silver-cored wires was evaluated in uniaxial tension, and in cyclic strain-controlled fatigue with the use of a flex tester operated to provide fully reversed bending fatigue. The magnitude of cyclic strains imparted to each cable tested was controlled via the use of different diameter mandrels. Smaller diameter mandrels produced higher values of cyclic strain and lower fatigue life. Multiple samples were tested and analyzed via scanning electron microscopy. The fatigue results were analyzed via a Coffin–Manson–Basquin approach and compared to fatigue data obtained on 316LVM cables where testing was conducted in an identical manner. The effects of changes in wire diameter, cable architecture, and wire composition (i.e. silver-cored vs. 316LVM) are discussed.

© 2008 Elsevier B.V. All rights reserved.

### 1. Introduction

A team of materials scientists at CWRU is supporting the development of a Networked Implantable Neuroprostheses System (NNPS) on an NIH-Bioengineering Research Partnership. The NNPS is being developed for application in the restoration of extremity function in patients with spinal cord injuries [1–4]. The Materials Group is leading the material and structural evaluation, analysis, and testing of implantable cables and interconnects that form part of the NNPS. The NNPS system relies on delivering operational power from a central power source to several remote devices via implantable-grade cables [5]. These implantable cables are constructed from small diameter wires for mechanical performance, while the high conductivity of the cables, ensures that power is delivered efficiently over these cables without undue transmission losses. In addition, the implantable cables must be reliable and withstand both static and cyclic loading for many years of implantation.

Previous studies have investigated the fatigue behavior of a range of wire/cable geometries and chemistries [6–10]. In the present study, the response of drawn filled tube (DFT<sup>®</sup>) (Fort Wayne Metals, Fort Wayne, IN) multi-strand cables to static and cyclic mechanical loading is reported. DFT<sup>®</sup> wires integrate the strength

and biocompatibility of implant grade alloys with desired properties of other materials. DFT<sup>®</sup> wires use the outer sheath to impart strength while the core material is designed to provide conductivity, radiopacity, resiliency, MRI enhancement, etc.

In this study helically wound DFT<sup>®</sup> cables with silver core surrounded by MP35N were evaluated. MP35N is a cobalt-based superalloy with composition (21%Cr, 35%Ni, 10%Mo, 25%Co). In the present work the silver core constitutes 41% of the cross-sectional area of the wire surrounded by MP35N. DFT<sup>®</sup> wire with 41% silver is 20 times more conductive than the 316LVM wire typically used in neuroprosthetic systems. In order to understand the factors affecting the performance of implantable cables made of such DFT<sup>®</sup> cables, their tensile and fatigue properties must be characterized. This work is part of a larger study investigating the fatigue behavior of a range of different candidate materials for use in next generation functional electrical stimulation (FES) systems.

Monotonic tensile tests were performed on the DFT<sup>®</sup> cables with different configurations and the fracture surfaces of the cables were examined under a scanning electron microscope (SEM) to reveal the fracture mechanisms involved. Fatigue testing was conducted using strain-controlled testing as conducted previously [10], in contrast to most previous work [6–9] conducted in rotating bending. For the NNPS implantable cables, fully reversed cyclic bending fatigue tests are physiologically more relevant than the rotating bending tests. Therefore, the DFT<sup>®</sup> cables were tested under fully reversed cyclic bending using a flex tester under various strain loading conditions.

\* Corresponding author. Fax: +1 2163683209.

E-mail address: [jjl3@case.edu](mailto:jjl3@case.edu) (J.J. Lewandowski).

**Table 1**  
Tensile properties of cables

Cable ID	Wire diameter (mm)	Cable diameter (mm)	0.2% offset yield stress $\sigma_y$ (MPa)	UTS (MPa)	Elastic modulus $E^a$ (GPa)	RA (%)	True fracture stress, $\sigma_f$ (MPa)	True fracture strain, $\varepsilon_f$	Elongation <sup>a</sup> (%)
DFT <sup>®</sup> 1 × 7(a)	0.038	0.114	1109	1148	194	29.3 ± 1.8	1624	0.35 ± 0.03	1.5
DFT <sup>®</sup> 1 × 7(b)	0.064	0.191	NA	NA	194	NA	NA	NA	NA
DFT <sup>®</sup> 7 × 7(a)	0.046	0.411	1051	1068	194	29.8 ± 3.7	1522	0.35 ± 0.05	3.3
DFT <sup>®</sup> 7 × 7(b)	0.058	0.526	1062	1226	194	24.6 ± 0.2	1626	0.28 ± 0.01	3.3
DFT <sup>®</sup> 7 × 19	0.036	0.533	808	1111	194	18.1 ± 3.6	1357	0.20 ± 0.04	4.6
316LVM 1 × 7 [10]	0.034	0.103	1135	1239	193	89.9 ± 3.8	5400 ± 1490	2.3 ± 0.3	1.9

<sup>a</sup> Data provided by the manufacturer.

The fatigue behavior of the cables observed experimentally was modeled using the Coffin–Manson–Basquin relationship as done previously [10].

## 2. Experimental procedures

### 2.1. Materials

Five DFT<sup>®</sup> cables with three different configurations viz. 1 × 7, 7 × 7 and 7 × 19 which comprise of 7, 49 and 133 individual DFT<sup>®</sup> wires, respectively, were examined in this study (Table 1). The diameter of individual wires range from 36 μm to 64 μm and the cable diameters range from 114 μm to 533 μm. All the cables were supplied by Fort Wayne Metals, Fort Wayne, IN.

### 2.2. Microhardness testing

Microhardness tests were conducted on both the Ag core and MP35N in the composite wire using a Buehler microhardness testing machine at 10 g load for the Ag and 10 g load for the MP35N. A DFT<sup>®</sup> 7 × 7 cable was first cross-sectioned and then mounted in an epoxy cold-mount, followed by metallographic polishing using SiC grit papers and then diamond paste and alumina slurries. Multiple indents were made in the Ag core and MP35N.

### 2.3. TEM and XRD

Transmission electron microscopy (TEM) was conducted on DFT<sup>®</sup> cable samples sectioned to reveal the MP35N, Ag core, and MP35N/Ag interface. The samples were prepared by first placing a DFT<sup>®</sup> 7 × 7 cable inside a ceramic tube just slightly larger than the diameter of the DFT<sup>®</sup> 7 × 7 cable, followed by sectioning perpendicular to the wire/cable axis to a 1-mm thickness using a slow speed diamond saw. The sections were then polished using SiC grit papers, followed by dimpling and then ion milling to produce an electron transparent foil that contained the MP35N, Ag core, and MP35N/Ag interface. These regions were analyzed using a Philips TEM to examine the grain size, interface integrity, and presence/absence of any interfacial reactions.

X-ray diffraction of the DFT<sup>®</sup> cables was accomplished on a Scintag X-1 advanced X-ray diffractometer (Scintag Inc., Cupertino, CA) using a scan rate of 0.05 °/s over the range of angles: 10–120°. DFT<sup>®</sup> 7 × 19 cables were positioned to completely cover a glass slide and XRD traces were taken at room temperature to determine the structure present in the as-received cables.

### 2.4. Tensile testing of the cables

All tensile tests were carried out to failure using a 25 mm span with displacement rate of 0.5 mm/min using a screw driven tabletop Instron Model 1130, Instron Corporation, Norwood, MA equipped with a 10-lb load cell and MTS Testworks software, MTS

Systems, Eden Prairie, MN. Both load and displacement were monitored via the MTS Testworks data acquisition system. The load vs. displacement data were analyzed using 0.2% offset for yield stress, while UTS was calculated at maximum load. Engineering stress was calculated using the applied load divided by the total area of the cable (i.e. number of wires × cross-sectional area of each wire). Elastic modulus was obtained from the manufacturer, while the reduction in area, RA, was determined by examining the final cross-sectional area of each of the wires in a Philips XL30 ESEM (Philips Electron Optics, Eindhoven, Netherlands) operated at 5 kV in secondary electron imaging mode. The true fracture strain,  $\varepsilon_f$ , and true fracture stress,  $\sigma_f$ , was calculated via Eqs. (1) and (2):

$$\varepsilon_f = \ln \left( \frac{100}{100 - \%RA} \right) \quad (1)$$

$$\sigma_f = \frac{P_f}{A_f} \quad (2)$$

where  $P_f$  is the fracture load of the 1 × 7 cable and  $A_f$  is the final cross-sectional area of the cable.

### 2.5. Fatigue testing

Fully reversed cyclic strain-controlled fatigue tests were carried out on the DFT<sup>®</sup> multi-strand cables using the flex tester described elsewhere [10]. The cable sample is placed between identically sized mandrels that are subjected to reciprocal movements in order to impose a fixed strain amplitude on the cable. A small break detector connected to the sample shuts off the machine when a current/voltage break is detected. A small dead load (e.g. 84 g) was used to keep the cable sample centrally located on the mandrels. All cables were tested at cyclic frequency of 1 Hz. In the present work, multiple tests were conducted at  $R = -1$  under different strain amplitudes by using mandrels of diameters ranging from 1.15 mm to 19.05 mm, as conducted previously [10].

Fatigue data were analyzed using Coffin–Manson–Basquin strain–life approach [11–13], whereby the total strain amplitude and fatigue life is given by

$$\frac{\Delta\varepsilon}{2} = \left( \frac{\sigma'_f}{E} \right) (2N_f)^b + \varepsilon'_f (2N_f)^c \quad (3)$$

where  $\Delta\varepsilon/2$  is the strain amplitude (half the total strain range),  $\sigma'_f$  is the fatigue strength coefficient,  $\varepsilon'_f$  is the fatigue ductility coefficient,  $b$  is the fatigue strength exponent,  $c$  is the fatigue ductility exponent and  $E$  is the elastic modulus [11–13]. This approach relates the uniaxial tensile behavior to the strain–fatigue life behavior. Since the strains and stresses for the straight core wire in the cable are higher than the helically twisted outer wires [8,14], bending of a helical cable over a mandrel can be approximated to bending of a slender rod over a radius of curvature. Considering pure bending of a thin straight wire of diameter around a well-defined and much larger radius, the cyclic strain range for fully reversed bending is

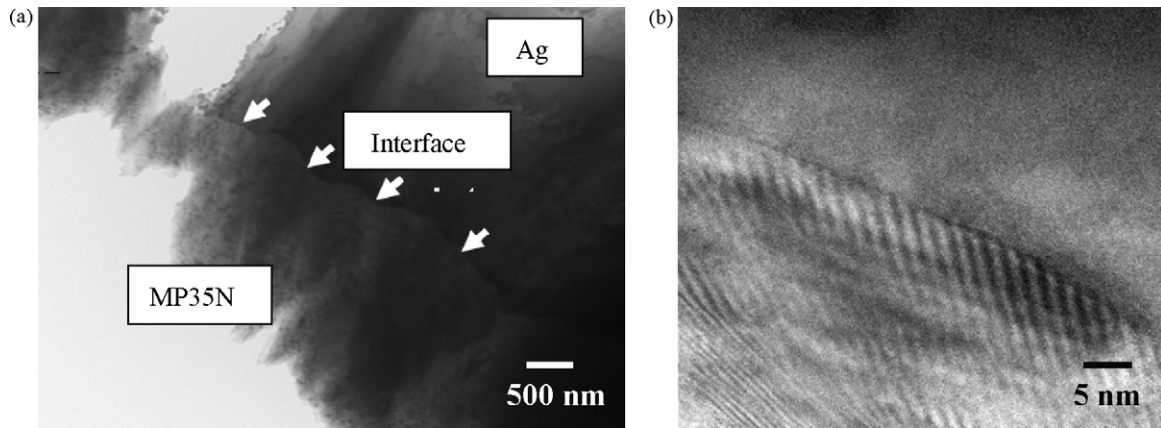


**Fig. 1.** TEM images at (a) low magnification and (b) higher magnification of interface between silver and MP35N. Ag/MP35N interface is absent of inclusions/particles and reaction layer and appears well bonded.

given by

$$\Delta\varepsilon = \frac{2\sigma}{E} = \frac{d}{\rho} \quad (4)$$

where  $d$  is the diameter of the individual wires in the cable and  $\rho$  is the mandrel radius.

Such an approach and analysis may be extended to other multi-strand cables, provided the diameter of the wires are significantly less than the bend radius provided by the mandrel [14]. It should be noted that, although these calculations provide a conservative estimate for the strain range in the cable, the contact stresses and the frictional dissipation between the wires in the cable are not included. While these stresses may affect the performance under certain loading conditions, a detailed analysis to account for contact and frictional stresses between the wires is beyond the scope of the present work and requires finite element modeling.

## 2.6. Fracture surface analysis

Fracture surfaces of the failed tension and fatigue samples were examined in a Philips XL30 ESEM operated at 5 kV. Tension samples were examined to determine the mechanism(s) of failure (e.g. dimpled fracture, ductile rupture, shear, etc.), while samples failed in fatigue were examined to determine the effect of cable configuration and size effects on fracture surface morphology. The microhardness indents obtained in Section 2.2 were also imaged using SEM.

## 3. Results

### 3.1. TEM observations and XRD results

TEM images from the DFT<sup>®</sup> 7 × 7 sample revealed an MP35N/Ag interface devoid of any particles/reactions and the interface appears to be well bonded in all areas examined (Fig. 1). Electron images of the Ag core revealed that it contained a low dislocation density and had very large grain size, in contrast to the MP35N where it was difficult to image individual grains. The XRD traces were sharp and revealed only peaks corresponding to an FCC structure, with  $d$ -spacings consistent with that of the MP35N [15].

### 3.2. Microhardness test results

Fig. 2a and b provides images of the indents in the Ag core and MP35N, respectively. The Vickers microhardness values obtained in the Ag and MP35N were  $0.63 \pm 0.05$  GPa and

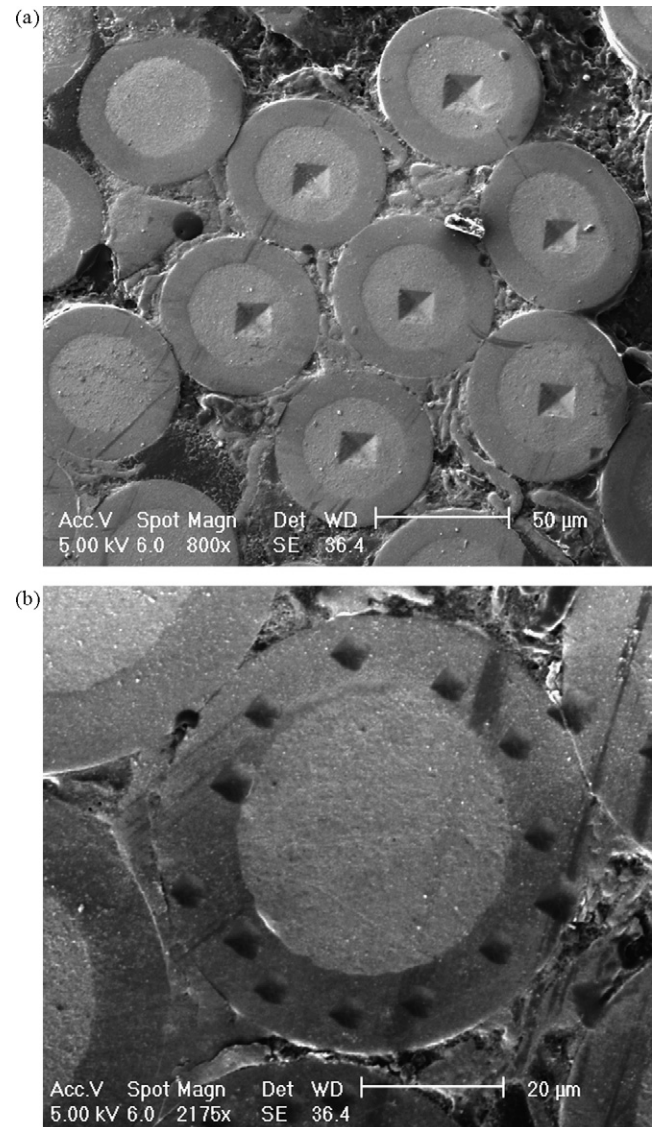


**Fig. 2.** SEM images of microhardness indentations in (a) silver core and (b) MP35N.

**Table 2**  
Effect of mandrel diameter on cycles to failure

Mandrel diameter (mm)	DFT® 1 × 7(a)	DFT® 1 × 7(b)	DFT® 7 × 7(a)	DFT® 7 × 7(b)	DFT® 7 × 19	316LVM 1 × 7 [10]
1.15	-	-	80	1,400	3,106	1145
1.15	-	-	99	-	592	1333
1.15	-	-	116	-	-	1647
1.15	-	-	-	-	-	1893
1.95	749	-	151	170	763	3088
1.95	1,155	-	155	3,675	-	3103
1.95	-	-	183	-	-	3171
1.95	-	-	-	-	-	3474
3.95	2,201	1,216	754	935	6,286	6818
3.95	-	-	765	-	6,456	9422
3.95	-	-	821	-	-	19355
3.95	-	-	926	-	-	-
3.95	-	-	1,083	-	-	-
3.95	-	-	1,257	-	-	-
5.92	16,360	18,509	3,033	5,360	19,660	20,837
5.92	-	-	4,219	-	55,397	23,993
5.92	-	-	-	-	-	45,227
7.92	30,005	59,373	24,073	36,848	486,065	265,792
7.92	-	72,924	47,885	-	491,500	-
7.92	-	-	52,787	-	-	-
7.92	-	-	60,565	-	-	-
9.88	113,160	33,934	2,254,910 (DNF)	360,000	-	1602123
12.6	442,430	32,918	2,702,004 (DNF)	2,511,100 (DNF)	2,348,902 (DNF)	2,710,000 (DNF)
12.6	-	43,395	-	-	-	-
19.05	1,065,245 (DNF)	1,111,600 (DNF)	-	-	-	-

DNF denotes sample did not fail after number of cycles listed. (a) and (b) refer to size of individual wires in cables tested, shown in Table 1.

6.03 ± 0.61 GPa, respectively. The Ag core was significantly softer than the MP35N shell, consistent with the differences in structure and dislocation density revealed by the TEM results shown in Fig. 1.

3.3. Tension tests

The tensile properties of the DFT® multi-strand cables are summarized in Table 1, while 316LVM 1 × 7 is provided for comparison. Similar UTS values were obtained despite the differences in the configuration and wire diameters of the five DFT® cables. In addition, the DFT® 1 × 7(a) cable with wire diameter 0.038 mm and 316LVM 1 × 7 cable exhibited similar tensile strengths and elastic modulus. However, the true fracture strain obtained from the reduction in area measurements of the DFT® 1 × 7(a) cable is only 15% of that of 316LVM 1 × 7 cable. The elongation to fracture of the two cables is similar since the large RA differences do not contribute much to the overall elongation (Table 1), and the uniform strains were similar.

3.4. Fatigue tests

The effect of changes in the mandrel diameter on the cycles to failure,  $N_f$ , is summarized in Fig. 3 and Table 2. An arrow indicates that the specimen did not fail after the number of cycles listed. As observed in 316LVM cables [10], the cycles to failure increased with an increase in the mandrel diameter for all the cables tested presently. This results because an increase in mandrel diameter imparts a smaller cyclic strain on the cable. The presently obtained flex-fatigue data are fitted to Coffin–Manson–Basquin relationship and is shown in Fig. 4 for the 1 × 7(a), 7 × 7(a) and 7 × 19 DFT® cables. The Coffin–Manson–Basquin curves presented in Fig. 4 are the best fit curves obtained by fitting Eq. (3) with the fatigue strength and ductility coefficients obtained from the tensile tests and manufacturer supplied elastic modulus (Table 1). The fatigue strength exponent and fatigue ductility exponent for the DFT® cables and the 316LVM 1 × 7 cable are presented in Table 3.

Flex-fatigue data for 316LVM 1 × 7 cables [10] are also included in Figs. 3 and 4 for comparison. Under high strain amplitude,

316LVM 1 × 7 cables performed better than all five DFT® cables. However, under low strain amplitude the DFT® 7 × 19 cable and 316LVM 1 × 7 cable performed similarly. The DFT® 1 × 7(a) cable and DFT® 7 × 7(a) cable performed worse than and better than

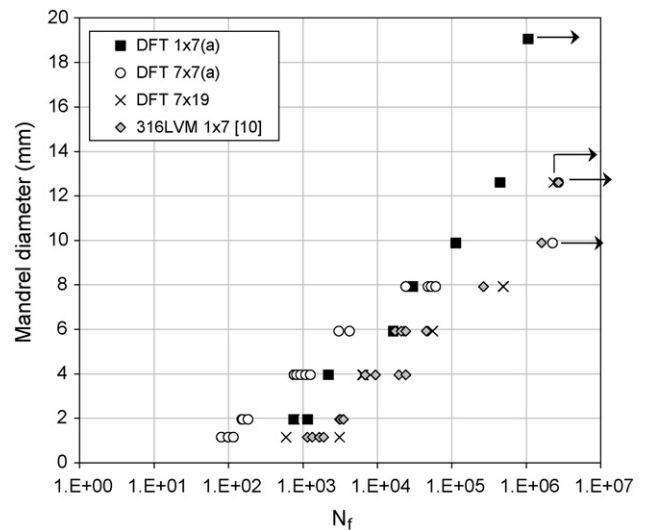
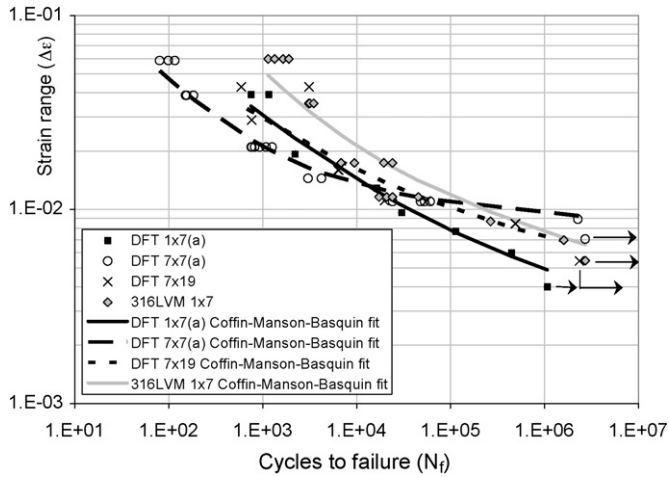


Fig. 3. Effect of mandrel diameter on the cycles to failure.

**Table 3**  
Fatigue strength and ductility exponents of cables

Cable ID	Fatigue strength exponent (b)	Fatigue ductility exponent (c)
DFT® 1 × 7(a)	-0.1	-0.45
DFT® 1 × 7(b)	-0.07	-0.44
DFT® 7 × 7(a)	-0.05	-0.6
DFT® 7 × 7(b)	-0.035	-0.52
DFT® 7 × 19	-0.06	-0.35
316LVM 1 × 7 [10]	-0.14	-0.65



**Fig. 4.** Strain-life behavior of DFT<sup>®</sup> cables and 316LVM 1 × 7 cable. The Coffin–Manson–Basquin relationship [11–13] was used to fit the data to Eq. (3) by using the uniaxial tension data obtained presently, Table 1. Arrows indicate sample did not fail.

316LVM 1 × 7 cable, respectively, under low strain amplitude (Fig. 4).

For a given mandrel size, the 7 × 19 cable exhibited higher cycles to failure ( $N_f$ ) as compared to other DFT<sup>®</sup> cables under high strain amplitude. The DFT<sup>®</sup> 1 × 7(a) cable exhibited slightly higher cycles to failure as compared to the 7 × 7(a) cable under high strain amplitude for a given mandrel size. However, the 7 × 7(a) cable exhibited higher cycles to failure as compared to the 1 × 7(a) cable under low strain amplitude for a given mandrel size (Fig. 3).

For a given cyclic strain range, both 1 × 7(a) and 7 × 19 cables exhibited similar cycles to failure under high strain amplitude. However, the 7 × 7(a) cable exhibited slightly lower cycles to failure under high strain amplitude as compared to 1 × 7(a) and 7 × 19 cables (Fig. 4). Under low strain amplitude, for a given cyclic strain range, the 7 × 7(a) cable exhibited the maximum cycles to failure followed by 7 × 19 and 1 × 7(a) cables (Fig. 4).

No significant effect of individual wire diameter was observed for either the 1 × 7 or 7 × 7 cables for a given mandrel size (Figs. 5 and 6). However, the 1 × 7(b) and 7 × 7(b) cables with a larger wire diameter exhibited higher cycles to failure for a given cyclic strain range (Figs. 7 and 8).

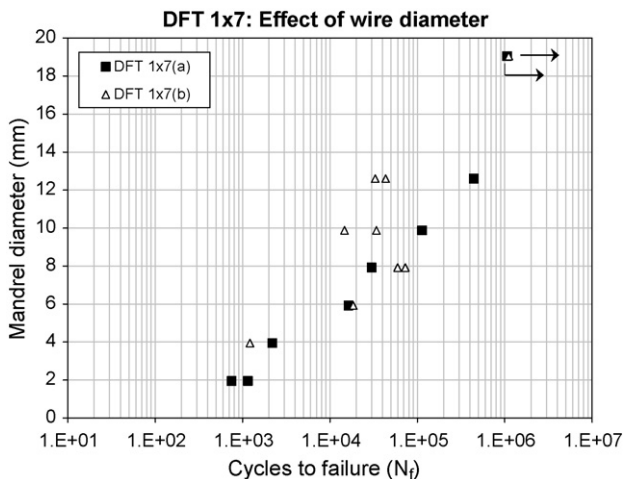


**Fig. 5.** Effect of mandrel diameter on the cycles to failure for DFT<sup>®</sup> 1 × 7 cables constructed of different wire diameters.

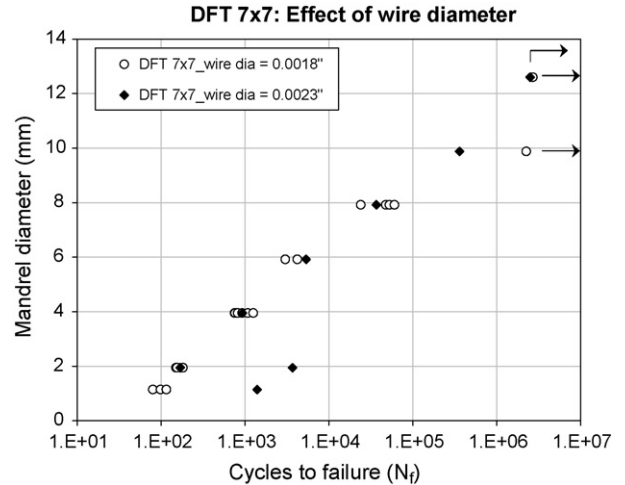


**Fig. 6.** Effect of mandrel diameter on the cycles to failure for DFT<sup>®</sup> 7 × 7 cables constructed of different wire diameters.

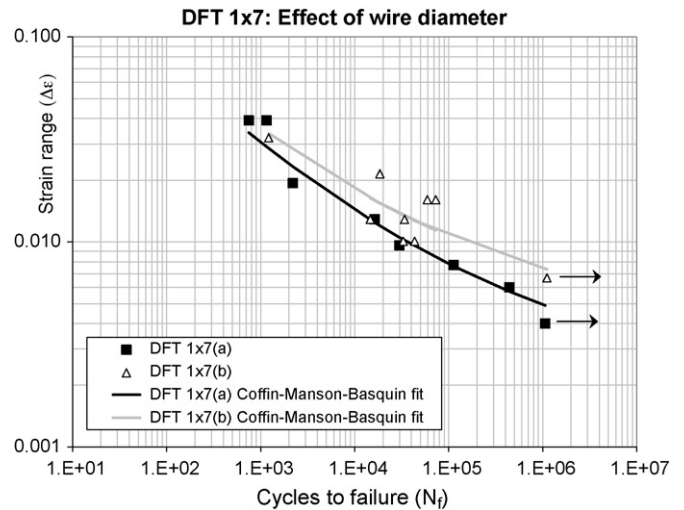


**Fig. 7.** Strain-life behavior of DFT<sup>®</sup> 1 × 7 cables constructed from different wire diameters. The Coffin–Manson–Basquin relationship [11–13] was used to fit the data to Eq. (3) by using the uniaxial tension data obtained presently, Table 1. Arrows indicate sample did not fail.

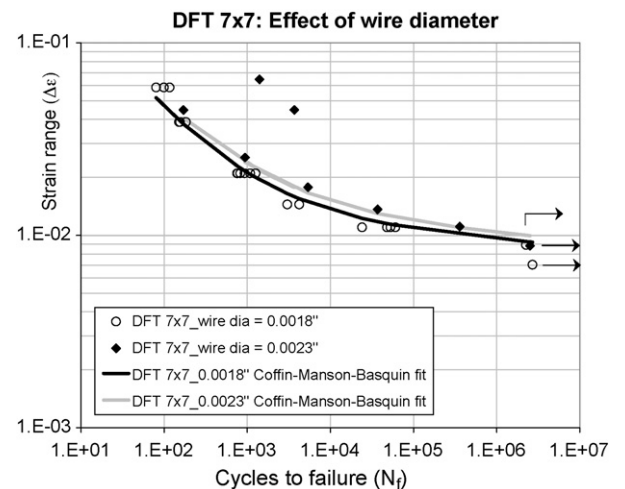


**Fig. 8.** Strain-life behavior of DFT<sup>®</sup> 7 × 7 cables constructed from different wire diameters. The Coffin–Manson–Basquin relationship [11–13] was used to fit the data to Eq. (3) by using the uniaxial tension data obtained presently, Table 1. Arrows indicate sample did not fail.

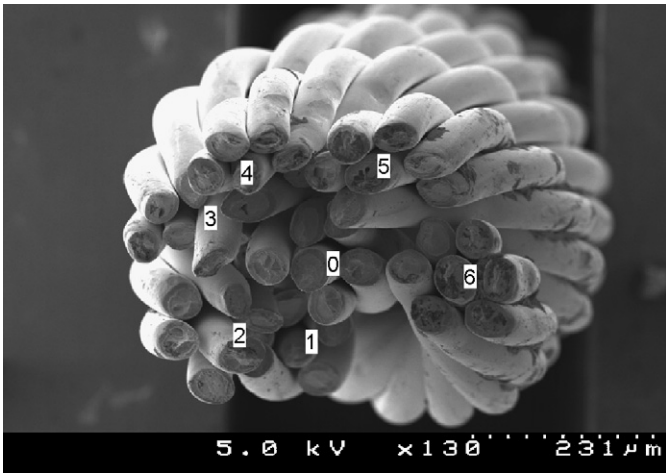


Fig. 9. Fracture surface of DFT® 7 × 7(a) cable tested in tension.

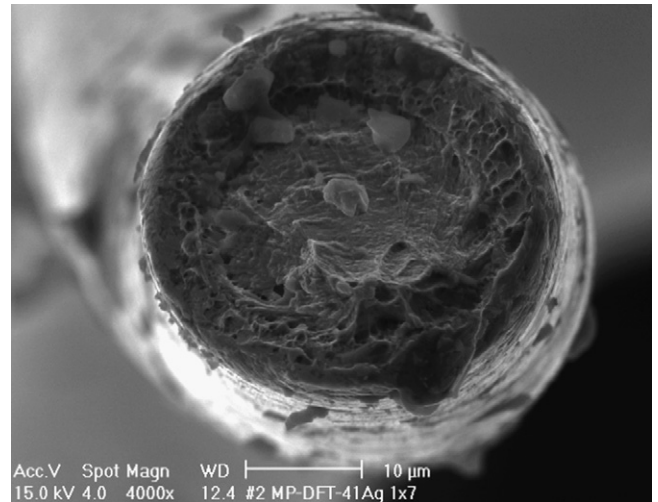


Fig. 11. High magnification view of fracture surface of an individual wire of DFT® 1 × 7(a) cable tested in tension.

3.5. Fracture surfaces

The fracture surface of each individual wire in the 316LVM 1 × 7 cable exhibited similar features, with extremely high reduction in area (e.g. ~90%) and a dimpled fracture surface as shown previously [10]. In contrast, representative fracture surfaces from the DFT® 7 × 7(a) cable tested in tension is shown in Figs. 9 and 10. The high magnification view shown in Fig. 10 indicates that both the MP35N and Ag core fail in a ductile manner, with dimples clearly present in both constituents, although the scale of the fracture surface features is somewhat different. There was no evidence of any interface debonding between the Ag core and MP35N in any of the individual wires in the 7 × 7 cables tested and examined. The remaining DFT® cables (i.e. 1 × 7 and 7 × 19) showed similar features (Figs. 11 and 12).

Representative fatigue fracture surfaces are shown in Figs. 13 and 14. High magnification views of the individual wires in the 7 × 7(a) cable reveal evidence of fatigue fracture in the individual wires comprising the cable, while fatigue initiation appeared to often occur at the contact points between each wire in the 7 × 7(a) cable. The remaining DFT® cables (i.e. 1 × 7 and 7 × 19) showed similar features.

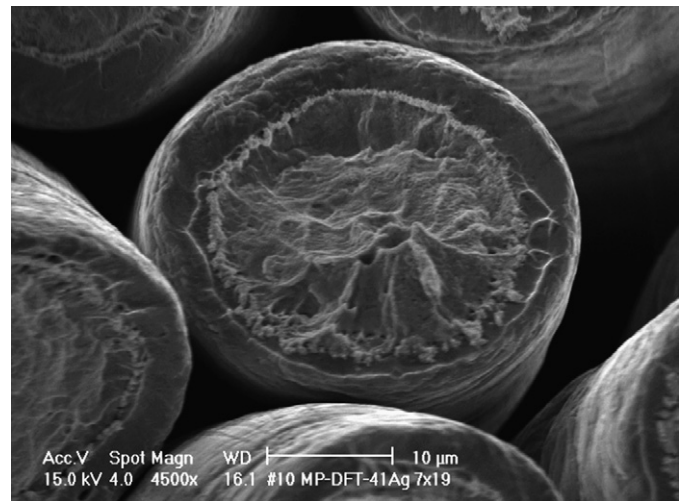


Fig. 12. High magnification view of fracture surface of an individual wire of DFT® 7 × 19 cable tested in tension.

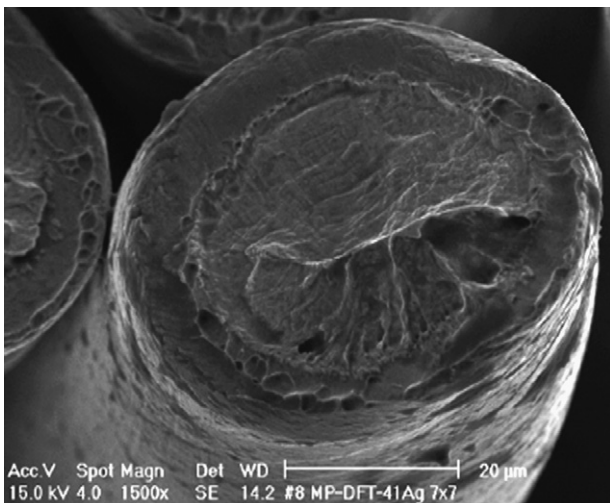


Fig. 10. High magnification view of fracture surface of an individual wire of DFT® 7 × 7(b) cable tested in tension.

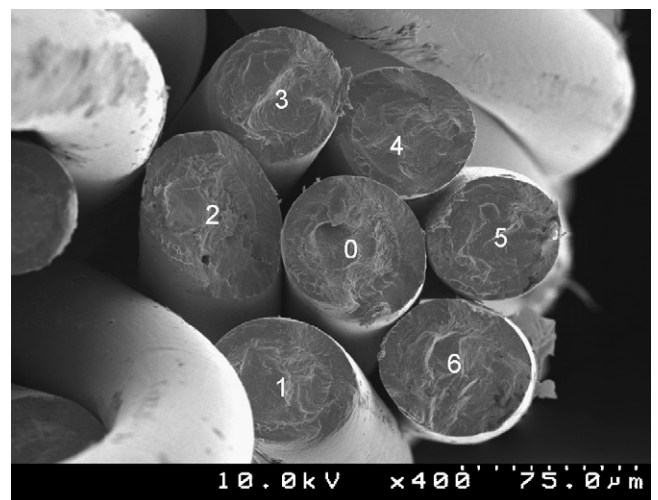
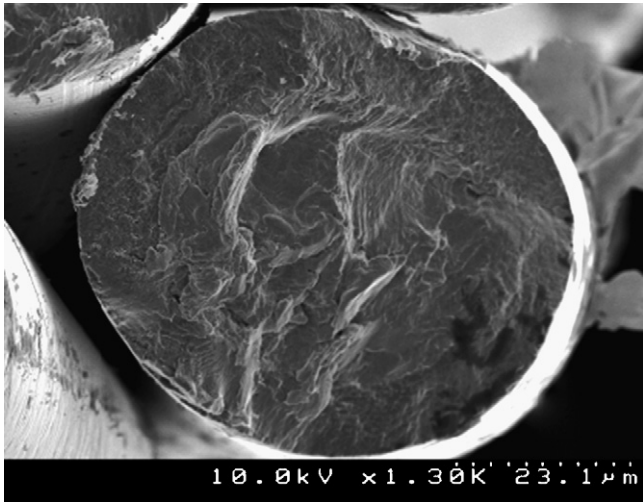


Fig. 13. Fatigue fracture surface of an individual strand of DFT® 7 × 7(a) cable.



**Fig. 14.** Magnified view of fatigue fracture surface of wire #6 (Fig. 13) from DFT<sup>®</sup> 7 × 7(a) cable.

**4. Discussion**

**4.1. Tensile properties**

The observation that the UTS of the cables are independent of cable configuration (i.e. 1 × 7, 7 × 7, and 7 × 19) indicates that the interactions between the constituent wires and strands of the cable do not play a significant role in the fracture of the cable under monotonic tension loading conditions. Thus the fracture of the cables under monotonic loading is primarily controlled by the fracture of the constituent wires and not the interactions between the wires.

The high tensile strength and ductility (i.e. RA and  $\epsilon_f$ ) exhibited by the 316LVM 1 × 7 cable is not unusual, as it is known that austenitic stainless steels are highly ductile, while the cold work imparted in the wire drawing process significantly increases the strength. The combination of high strength and high ductility has been demonstrated in a number of drawn wires, including patented steel wire, as reviewed elsewhere [16]. For comparison, handbook values for annealed AISI 316LN are yield stress-205 MPa, UTS-515 MPa, RA-60% [17]. The DFT<sup>®</sup> wires also exhibited very high tensile strength levels as shown in Table 1, despite the presence of the soft Ag core. The microhardness of the Ag core,  $0.63 \pm 0.05$  GPa converts to a strength of about 210 MPa, while that of the MP35N shell (i.e.  $6.03 \pm 0.61$  GPa) converts to a strength of about 2000 MPa. The TEM images revealed a much larger grain size and very low dislocation density in the Ag core, consistent with its low microhardness. In considering the microhardness of the MP35N shell, microhardness values ( $H_v$ ) of upto 4.6 GPa were observed in 80% cold worked, 0.16 mm-thick MP35N sheets [18]. In another recent study by Yu et al. [19], microhardness of up to 8 GPa was observed for a fine 203 μm diameter MP35N wire. The microhardness values obtained in this study (6.3 GPa) are greater than that reported by cold work alone, while the XRD results revealed only FCC structure present. In related work, work-hardening of multi-phase Cobalt–Nickel alloys has been attributed to formation of stress-induced hexagonal-close-packed (HCP) platelets in the FCC matrix and production of primary deformation twins [20,21]. Twin boundaries and platelets formed during a wire drawing process could possibly provide additional barriers for dislocation motion and result in increase in microhardness and strength. However, for alloys with Co:Ni ratio less than 45:25, it is not possible to detect stress-induced formation of HCP phase by X-diffraction techniques [18]. In a 33:36 alloy the size of the platelets were observed to be

too thin to provide sufficient intensity in the diffraction patterns [18]. The MP35N alloy used in this study has Co:Ni of 25:35. XRD spectra obtained for the present MP35N alloy revealed characteristics similar to earlier studies [18]. Only FCC peaks were observed and no peaks corresponding to HCP structure were obtained.

It is also clear from the TEM and SEM results that the Ag core is well bonded to the MP35N shell and it does not debond during deformation and fracture of the wire, either in monotonic or cyclic loading. This also partly explains why DFT<sup>®</sup> wires exhibited less RA in comparison to 316LVM, which is predominantly due to the larger non-uniform strain in the 316LVM wire. Although Ag is typically highly ductile, but low in strength, the lower RA of the DFT<sup>®</sup> composite wire is partly due to the high constraint of the Ag core by stronger MP35N shell, similar to recent constrained flow experiments of various metals [22,23]. The lack of interface debonding between the MP35N and Ag core produces very high constraint in the Ag core, thereby elevating the stresses in the Ag core and accelerating the stages of ductile fracture. The resulting fracture surface of the Ag core is still locally ductile, but occurs at a lower global strain than that would be experienced in a smooth tension test on Ag alone due to the high tensile constraint (i.e. high hydrostatic tensile stress) [24].

**4.2. Fatigue behavior**

Although the tensile strengths of the various cables were not significantly affected by changes to the cable architecture (i.e. 1 × 7 vs. 7 × 19 vs. 7 × 7) or to changes in the wire diameter, the fatigue performance under the flex bending fatigue conditions utilized presently exhibited significant effects of cable architecture and measurable effects of wire diameter. In order to facilitate discussion, the fatigue performance is provided as a ranking from highest (i.e. most cycles to failure) to lowest (i.e. fewest cycles to failure) in Table 4. Since cables containing wires of different diameter were tested presently, the rankings in Table 4 are provided using both the mandrel diameter (e.g. using data from Figs. 3, 5, 6) and cyclic strain (e.g. using data from Figs. 4, 7, 8). In addition, the performance is also ranked for the low cycle fatigue regime (e.g. cycles to failure <10,000) as well as the high cycle regime (e.g. cycles to failure >100,000).

Table 4 reveals that the 316LVM 1 × 7 cable performs best under low cycle fatigue conditions (i.e. small mandrel diameter, large cyclic strains). This is consistent with much previous work [11–13,25,26] on conventional structural materials since the highest tensile strain to failure was exhibited by the 316LVM 1 × 7 in comparison to all of the other materials tested. In contrast, both DFT<sup>®</sup> 7 × 7 cables exhibited shorter lifetimes in the low cycle regime, consistent with the much lower ductility of these cables.

In the high cycle fatigue regime (i.e. large mandrel diameter, low cyclic strains) both DFT<sup>®</sup> 7 × 7 cables performed better than all of the other cables tested. Although this may appear inconsistent with the similar tensile strengths exhibited by the DFT<sup>®</sup> 7 × 7 and 316LVM 1 × 7 (Table 1), the flex bending fatigue tests subject the

**Table 4**  
Ranking of flex bending fatigue performance of cables tested presently

Mandrel size vs. $N_f$		$\Delta\epsilon$ vs. $N_f$	
LCF	HCF	HCF	LCF
316LVM 1 × 7	DFT <sup>®</sup> 7 × 7(a)	DFT <sup>®</sup> 7 × 7(b)	316LVM 1 × 7
DFT <sup>®</sup> 7 × 19	DFT <sup>®</sup> 7 × 7(b)	DFT <sup>®</sup> 7 × 7(a)	DFT <sup>®</sup> 7 × 19
DFT <sup>®</sup> 1 × 7(a)	316LVM 1 × 7	316LVM 1 × 7	DFT <sup>®</sup> 1 × 7(a)
DFT <sup>®</sup> 1 × 7(b)	DFT <sup>®</sup> 7 × 19	DFT <sup>®</sup> 7 × 19	DFT <sup>®</sup> 1 × 7(b)
DFT <sup>®</sup> 7 × 7(a)	DFT <sup>®</sup> 1 × 7(a)	DFT <sup>®</sup> 1 × 7(b)	DFT <sup>®</sup> 7 × 7(b)
DFT <sup>®</sup> 7 × 7(b)	DFT <sup>®</sup> 1 × 7(b)	DFT <sup>®</sup> 1 × 7(a)	DFT <sup>®</sup> 7 × 7(a)

outer surfaces of the wires to cyclic strain/stress and not the whole wire diameter. In that regard, the microhardness tests revealed the MP35N to possess hardness in excess of 6 GPa, providing an estimated tensile strength in excess of 2 GPa for the MP35N shell. This is significantly higher than the hardness/strength of the 316LVM  $1 \times 7$  and is consistent with much previous work that shows that fatigue life in the high(er) cycle regime is controlled by strength level [11–13,25,26]. The larger number of cycles to failure exhibited by the DFT<sup>®</sup>  $7 \times 7$  cables in the high cycle regime is thus consistent with the higher hardness/strength of the outer MP35N shell compared to the 316LVM  $1 \times 7$  cables.

The effects of changes in wire diameter on the flex bending fatigue performance are provided in Figs. 5 and 7 for DFT<sup>®</sup>  $1 \times 7$ , and in Figs. 6 and 8 for DFT<sup>®</sup>  $7 \times 7$ . The cables with thinner wires for both the  $1 \times 7$  and  $7 \times 7$  DFT<sup>®</sup> cables exhibit longer fatigue life for both high cycle (i.e. large mandrel and small strain amplitude) and low cycle (i.e. small mandrel and large strain amplitude) conditions. In part, this results from the smaller strain amplitude imparted to smaller diameter wires (in comparison to larger diameter wires) when the same mandrel size is used for the flex bending fatigue test, as predicted in Eq. (4). Less of a difference between the thinner and thicker wires is obtained when the data are plotted using cyclic strain amplitude vs. cycles to failure where the thicker wires show somewhat better performance over the range of cyclic strains tested.

Analyses of the fatigue and tension data using the Coffin–Manson–Basquin approach produced values for  $b$  and  $c$  (Table 2) consistent with that exhibited by most engineering metals [11–13,25,26]. For example, the fatigue strength exponent and fatigue ductility exponent ranges from  $-0.14$  to  $-0.05$  and from  $-0.8$  to  $-0.5$ , respectively.

Examination of cables fatigued to failure revealed similar fracture surface features. Fatigue fracture initiation often appeared to occur at the contact points between each wire in the cable. Evidence of sequential failure was observed in each of the wires, similar to that reported previously for the 316LVM  $1 \times 7$  cable [10]. There was no evidence of debonding between the MP35N and Ag core.

## 5. Conclusions

The mechanical behavior of DFT<sup>®</sup> cables with various configurations was evaluated in uniaxial tension and in fully reversed cyclic strain-controlled flex bending fatigue. Cyclic strains were controlled via the use of different diameter mandrels. The pertinent conclusions are as follows:

1. Microstructural analyses of the Ag core in as-received DFT<sup>®</sup> cables exhibited a low dislocation density and very large grain size. XRD of as-received DFT<sup>®</sup> cables revealed the MP35N outer shell to possess a FCC structure. Microhardness measurements of the MP35N shell revealed hardness in excess of 6 GPa while the Ag core exhibited a hardness of only 0.6 GPa. TEM analyses revealed the Ag/MP35N interface to be well bonded, with no evidence of any precipitation/phases at the interface.
2. Tension tests performed on the various DFT<sup>®</sup> cables revealed that each of the cables exhibited tensile strength in excess of 1000 MPa despite the presence of the soft Ag core. No evidence of interface (i.e. MP35N/Ag) debonding was obtained in any of the tension or fatigue experiments. Variations in cable architecture (e.g.  $1 \times 7$ ,  $7 \times 7$ , and  $7 \times 19$ ) did not exert a significant effect on the tensile properties measured, indicating that the contact points between wires did not significantly affect the tensile properties. The fracture strains of the DFT<sup>®</sup> cables were less than 0.3 (i.e. reduction in area <30%) with little evidence of post-necking

strain, in contrast to the high reduction in area (e.g. >95%) exhibited by the 316LVM  $1 \times 7$  cables.

3. The flex bending fatigue performance of DFT<sup>®</sup> cables tested under fully reversed cyclic strain controlled conditions revealed significant effects of cable architecture (e.g.  $1 \times 7$ ,  $7 \times 7$ , and  $7 \times 19$ ) with more moderate effects of changes in wire diameter for a given architecture. The high ductility of the 316LVM  $1 \times 7$  produced the best performance under low cycle fatigue conditions (i.e. small mandrel diameter and high cyclic strains) while the higher strength  $7 \times 7$  DFT<sup>®</sup> cables performed the best under the high cycle fatigue conditions (e.g. large mandrel diameter and low cyclic strain). The data were analyzed using the Coffin–Manson–Basquin approach and produced values for the fatigue strength coefficient,  $b$ , and fatigue ductility coefficient,  $c$ , consistent with those for conventional structural materials.
4. Fracture surface analyses revealed that fatigue fracture initiation typically occurred at the contact points between wires in the various cables. Evidence of fracture surface features consistent with fatigue fracture was obtained in all of the cables examined. There was no evidence of debonding between the MP35N and Ag core.

## Acknowledgements

This research is supported by NIH-NINDS Grant No. NS-041809 and NIH-NIBIB Grant No. EB-001740. Principal Investigator P. Hunter Peckham. The authors appreciate Chris Tuma, Luciano O. Vatamanu, Mostafa Shazly, Dingqiang Li and Joshua Caris for their help with mechanical testing, microhardness measurements, electron microscopy and XRD. The authors also appreciate discussions with various members of the Functional Electrical Stimulation (FES) Center housed at CWRU.

## References

- [1] Y. Handa, Proceedings of the IEEE Engineering in Medicine and Biology Conference, 1987.
- [2] K.R. Marsolais, Proceedings of the 8th Annual RESNA Conference, 1985.
- [3] P.H. Peckham, E.B. Marsolais, J.T. Mortimer, J. Hand Surg. 5 (1980) 462–469.
- [4] A. Scheiner, E.B. Marsolais, Proceedings of the 13th Annual RESNA Conference, 1990.
- [5] B. Smith, T.J. Crish, J.R. Buckett, K.L. Kilgore, P.H. Peckham, Proceedings of the 2nd International IEEE EMBS Conference on Neural Engineering, 2005.
- [6] P.A. Altman, J.M. Meagher, D.W. Walsh, D.A. Hoffmann, J. Biomed. Mat. Res., App. Biomater. 43 (1) (1997) 21–37.
- [7] Y. Iguchi, T. Narushima, K. Suzuki, M. Watanabe, T. Kinami, T. Nishikawa, N. Hoshimiya, Y. Handa, Proceedings of the International Functional Electrical Stimulation Society, 2000.
- [8] A. Meyer, MS thesis, Mechanical and Aerospace Engineering, Case Western Reserve University, Cleveland, 1985.
- [9] A. Scheiner, J.T. Mortimer, T.P. Kicher, J. Biomed. Mater. Res. 25 (1991) 589–608.
- [10] J.J. Lewandowski, R. Varadarajan, B. Smith, C. Tuma, M. Shazly, L.O. Vatamanu, Mater. Sci. Eng. A 486 (2008) 447–454.
- [11] S.S. Manson, Mach. Des. 21 (1960) 139–144.
- [12] L.F. Coffin, J.F. Tavernelli, Trans. AIME 215 (1959) 794–807.
- [13] S.S. Manson, M.H. Hirschberg, Fatigue: An Interdisciplinary Approach, Syracuse University Press, Syracuse, New York, 1964.
- [14] G. Costello, Theory of Wire Rope. Mechanical Engineering Series, second ed., Springer, New York, 1997.
- [15] Y.J. Graham, A.H. Youngblood, Met. Trans. 1 (1970) 423–430.
- [16] E.M. Taleff, J.J. Lewandowski, B. Poulodan, J. TMS Soc. 54 (7) (2002) 25–30.
- [17] Metals Handbook, Desk edition, ASM, Materials Park, OH, 1985.
- [18] A. Ishmaku, K. Han, Mater. Charact. 47 (2001) 139–148.
- [19] N. Yu, A.A. Polycarpou, A.J. Wagoner Johnson, J. Biomed. Mater. Res. Part B: Appl. Biomater. 70B (2003) 106–113.
- [20] R.P. Singh, R.D. Doherty, Met. Trans. 23A (1992) 321–334.
- [21] E. El-Danaf, S.R. Kalidini, R.D. Doherty, Met. Mater. Trans. 30A (1999) 1223–1233.
- [22] J. Kajuch, J.W. Short, J.J. Lewandowski, Acta Metall. Mater. 43 (1995) 1955–1967.
- [23] M.F. Ashby, F.J. Blunt, M. Bannister, Acta Metall. 37 (7) (1989) 1847–1857.
- [24] J.J. Lewandowski, P. Lowhaphandu, Int. Mater. Rev. 43 (4) (1998) 145–187.
- [25] M.R. Mitchell, Fatigue and Microstructure, ASM Materials Park, Ohio, 1978, pp. 385–438.
- [26] N.E. Dowling, Mechanical Behavior of Materials, Prentice Hall, Upper Saddle River, NJ, 1998.